Draft version August 11, 2025
Typeset using LaTeX twocolumn style in AASTeX631

Stellar Evolution with Radiative Feedback in AGN Disks

Zheng-Hao Xu,[1] Yi-Xian Chen,[2] and Douglas N. C. Lin[3,4,5]

[1] Department of Physics, University of California Santa Barbara, Santa Barbara, CA, 93106, USA
[2] Department of Astrophysics, Princeton University, Princeton, NJ, 08544, USA
[3] Department of Astronomy and Astrophysics, University of California, Santa Cruz, CA, 95064, USA
[4] Institute for Advanced Study, Tsinghua University, Beijing, 100084, China
[5] Department of Astronomy, Westlake University, Hangzhou, Zhejiang, 310030, China

ABSTRACT

Stars embedded in the ∼pc region of an active galactic nucleus (AGN) experience extreme accretion conditions that significantly alter their evolution. We present one-dimensional MESA simulations of stars growing and decaying within AGN disks, implementing radiative-feedback-regulated accretion, limiting stellar growth near the Eddington luminosity, as well as wind-driven mass loss. Unlike standalone stars in the field, these embedded stars follow unique evolutionary tracks with well-determined mass evolution and chemical yields. We distinguish two regimes: "immortal" stars that indefinitely remain on the main sequence due to efficient hydrogen mixing; and "metamorphic" stars whose growth is limited by feedback, ultimately enriching the disk with heavy elements upon hydrogen and helium exhaustion in their cores. Results indicate that embedded stars in AGN disks can attain large masses, but radiative feedback, gas retention and limited mixing likely ensure the "immortal" track is unsustainable. Embedded metamorphic stars significantly enrich AGN disks with helium and α-elements, potentially explaining the observed high metallicity in broad-line regions (BLR) without excessive helium enrichment. This study underscores the critical interplay between stellar feedback and accretion physics in shaping the stellar populations and chemical evolution within AGN disks.

Keywords: active galactic nuclei — stellar evolution — radiative feedback — mass loss — chemical enrichment

1. INTRODUCTION

Accretion disks in active galactic nuclei (AGNs) provide environments with extreme density and radiation fields. In the dense gas of an AGN disk, stars can form in situ via disk fragmentation (Goodman & Tan 2004; Jiang & Goodman 2011; Chen et al. 2023) or be captured from the nuclear star cluster (Artymowicz et al. 1993; MacLeod & Lin 2020; Wang et al. 2024). Once formed or embedded, these stars are immersed in gas with densities $\rho \sim 10^{-20}$–10^{-10} g cm^{-3} and temperatures $T \sim 10^3$–10^6 K, which are orders of magnitude higher than those in typical interstellar environments (Cantiello et al. 2021). Their energy output may help sustain the extended, self-gravitating disk structure (Sirko & Goodman 2003; Thompson et al. 2005; Chen & Lin 2024), potentially relevant to the infrared emission in 'Little Red Dots' (Zhang et al. 2025).

Several lines of evidence support the survival and growth of stars within AGN disks. Emission lines from the broad-line region (BLR) consistently show redshift-independent, super-solar metallicities (Hamann & Ferland 1999; Hamann et al. 2002; Nagao et al. 2006; Xu et al. 2018; Wang et al. 2022; Huang et al. 2023), possibly due to enrichment from local stellar populations (Ali-Dib & Lin 2023; Fryer et al. 2025). Stars in AGN disks may also serve as progenitors of gravitational wave sources, either through stellar mergers or the formation of massive black hole binaries within the disk (McKernan et al. 2012; Graham et al. 2020; Tagawa et al. 2020; Samsing et al. 2022), when direct capture of compact objects is less efficient (MacLeod & Lin 2020).

Regarding these scenarios, the extent to which massive stars contribute to the metallicity of AGN disks and evolve off the main sequence depends sensitively on their poorly understood evolution in the gas-rich AGN environment. Jermyn et al. (2022) proposed that such stars might become "immortal" if the hydrogen-rich accreted gas can efficiently diffuse through the radiative zone (upper branch, Fig. 1), such that they continuously burn hydrogen over the AGN's lifetime. These immortal stars could steadily burn hydrogen near the Eddington limit, influencing the disk's chemical composition by converting hydrogen into helium (and potentially releasing it back into the disk). However, this raises a critical question: while AGN broad-line regions exhibit enhanced metallicities, particularly in α-elements and iron, they do not show the extreme helium enrichment (Huang et al. 2023) that would be expected if immortal stars were common.

More broadly, using accretion and stellar wind prescriptions within one-dimensional stellar evolution models, Dittmann et al. (2021); Fabj et al. (2025) conducted parameter surveys across typical AGN disk environments and found that stellar evolution outcomes vary widely depending on the local gas density. In high-density regions, stars can not only become fully immortal, but also their Kelvin–Helmholtz timescale may fall below the mass doubling timescale, triggering runaway growth toward pair-instability supernovae and/or intermediate-mass Black Holes. Even a small number of such supermassive stars could dramatically alter disk properties—making it difficult to reconcile their existence with the lack of corresponding observational signatures from AGNs.

However, a key physical ingredient missing from these studies is a self-consistent treatment of radiative feedback. Recent hydrodynamic simulations in Chen et al. (2024, 2025) demonstrate that when full radiative transfer is included, the accretion rate onto stars is limited by Eddington feedback: once the accretion luminosity approaches the star's Eddington luminosity, radiation force suppresses further infall. This significantly reduces the stars' actual accretion rate compared to the Bondi rate usually assumed in 1D studies, placing a fundamental limit on stellar growth in AGN disks, similar to the Eddington limit for black holes (lower branch, Fig. 1).

In this work, we present the Stellar Evolution and Pollution in AGN Disks (SEPAD) model that incorporates an updated treatment of radiative feedback. We show that this mechanism plays a critical role in preventing runaway growth in high-density environments. We emphasize that once stars reach high luminosities, their accretion becomes limited by the Eddington rate, making it effectively *independent* of the background gas density. Figure 1 outlines the feedback-regulated evolution of a star embedded in an AGN disk and how it might pollute the disk.

The paper is organized as follows: In §2, we develop a theoretical framework for accretion onto stars embedded in AGN disks, including Bondi accretion estimates, radiative feedback limits, and semi-analytical estimates for stellar quasi-equilibrium masses. In §3, we describe our numerical approach using MESA, detail the modifications made to the accretion and wind routines from Cantiello et al. (2021), and explain our implementation of mixing processes within the radiative zones. In §4, we present results from representative simulations, examining stellar mass growth across different conditions, the interplay between accretion and wind mass loss, average luminosity and Eddington ratios, surface composition evolution, and the final stellar outcomes. Finally, in §5, we summarize our key conclusions, discuss the broader implications of our findings for observations, including their relevance to BLR emission properties and the overall energy budget of AGN disks.and suggest directions for future work.

2. ANALYTICAL EXPECTATIONS

In this section, we develop the theoretical framework for a star evolving in an AGN–disk, highlighting the key physical processes: **the dependency of Helium fraction, accretion from the disk, radiative feedback, and stellar–wind mass loss**, and aim to derive simple conclusions that we can test with numerical simulations. We begin by describing the AGN–disk environment and the baseline Bondi accretion rate onto the star (§2.1). We then introduce how radiative feedback imposes an Eddington-limited accretion rate (§2.2) and how we implement a suppression factor $S_{\lambda_0}(\lambda_\star)$ to smoothly regulate accretion as the star approaches this limit. Next, we discuss the onset of continuum-driven stellar winds when the star's luminosity is near Eddington (§2.3) and explore the condition for quasi accretion–wind equilibrium (§2.4). If an equilibrium is reached, the star can maintain a steady mass (potentially becoming an "immortal" main–sequence star), but if not, the star will eventually enter a mass-losing post-main–sequence evolution and die ("metamorphic" evolution), with important consequences for mixing and chemical yields.

2.1. *Accretion in an AGN disk: Baseline Rates*

The outer self-gravitating, star-forming region of an AGN may be approximated by a simple constant α and constant Q disk model (Sirko & Goodman 2003; MacLeod & Lin 2020; Chen & Lin 2024). With an α prescription for accretion rate, an accretion disk attains a steady state with a constant accretion rate

$$\dot{M}_{\rm d} = \frac{3\alpha h^3}{Q} M_\bullet \Omega = \frac{3\alpha c_{\rm s}^3}{GQ} \tag{1}$$

where $c_{\rm s}$ is the mid-plane sound speed of the disk gas and radiation, $M_\bullet$ and $m_8 = M_\bullet/10^8 M_\odot$ are the mass and normalized mass of the SMBH. In terms of the gravitational stability parameter $Q = c_{\rm s}\Omega/\pi G\Sigma \sim 1$, the midplane density

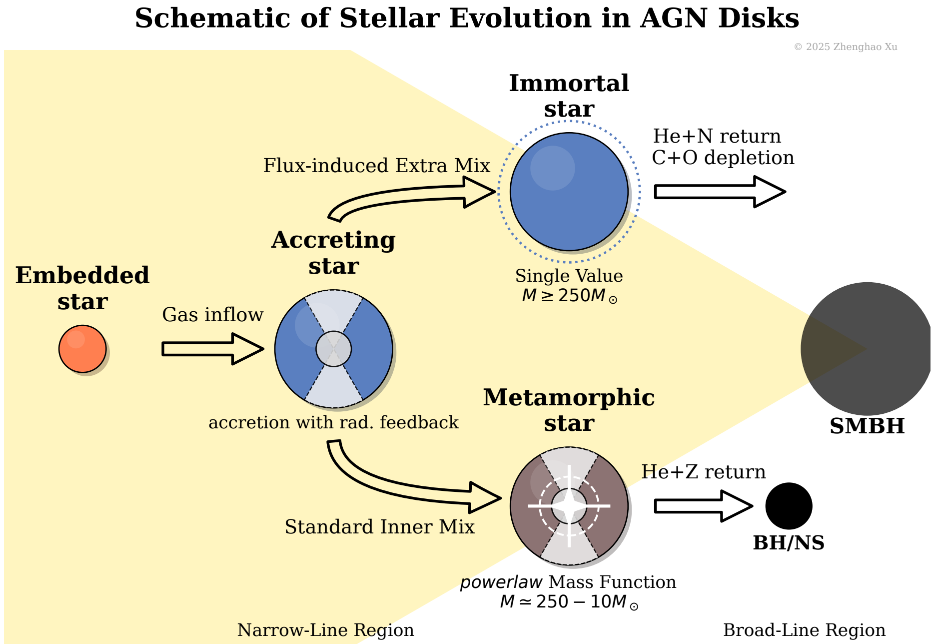

Figure 1. Diagram of a star embedded in an AGN accretion disk. Gas from the disk feeds the star at a Bondi–Hoyle rate; radiative feedback limits the net supply as soon as the stellar luminosity approaches a fraction $\lambda_0 \, L_{\rm Edd}$. Excess energy powers a wind that removes both mass and angular momentum. (Upper branch: immortal stars) radiation-flux–induced internal mixing feeds fresh H and dredges He, keeping the star on the main sequence; CNO cycling enriches N and depletes C and O. (Lower branch: metamorphic stars) without this extra mixing, the star evolves off the main sequence. Moreover, it returns metal-rich winds that match the super-solar abundances observed in the Broad-Line Region spectra.

$$\rho_c = \frac{M_\bullet}{2\pi Q R^3} = \frac{10^{-15}}{Q}\frac{m_8}{r_{\rm pc}^3}\frac{\rm g}{cm^3} = \frac{10}{Q m_8^2}\frac{R_\bullet^3}{R^3}\frac{\rm g}{cm^3} \tag{2}$$

where R and $r_{\rm pc} = R/1{\rm pc}$ are the physical and normalized radius, $R_\bullet = GM_\bullet/c^2$ is the SMBH's gravitational radius. For luminous AGNs,

$$\dot{M}_\bullet \simeq 2 m_8 \frac{\lambda_{\bullet 6}}{\epsilon_{\bullet 06}}\frac{M_\odot}{\rm yr} \tag{3}$$

where $\lambda_\bullet = L_\bullet / L_{{\rm Edd},\bullet}$ and $\epsilon_\bullet$ are SMBH's Eddington and efficiency factors, $\lambda_{\bullet 6} = \lambda_\bullet/0.6$ and $\epsilon_{\bullet 06} = \epsilon_\bullet/0.06$ are normalized by their mean values inferred from the evolution of AGN's luminosity function (Yu & Tremaine 2002; Shankar et al. 2009). SMBH's Eddington luminosity limit is $L_{{\rm Edd},\bullet} = 4\pi G M_\bullet m_p c/\sigma = 1.26\times 10^{46} m_8 {\rm erg\ s^{-1}}$. If Q and α are constant, the radiation-pressure dominated sound speed ($c_{\rm s} \approx c_{\rm s,rad}$) is nearly constant,

$$c_{\rm s,rad} = \left(\frac{QG\dot{M}_\bullet}{3\alpha}\right)^{1/3} = 14\left(\frac{m_8 \lambda_{\bullet 6}}{\epsilon_{\bullet 06}}\right)^{1/3}\frac{\rm km}{\rm s}. \tag{4}$$

with mid-plane temperature

$$\rho_c c_{\rm s,rad}^2 = \frac{a}{3} T_c^4. \tag{5}$$

To verify self-consistency, we find the ratio of radiation to gas pressure in the mid-plane:

$$\Pi = \frac{c_{\rm s,rad}^2}{c_{\rm s,gas}^2} = \frac{\mu a (3\rho c_{\rm s,rad}^2/a)^{3/4}}{3\rho\mathcal{R}} = 15 Q^{1/4} m_8^{1/4} \frac{\lambda_{\bullet 6}^{1/2}}{\epsilon_{\bullet 06}^{1/2}} r_{\rm pc}^{3/4} \tag{6}$$

increases with R and exceeds unity (radiation pressure dominant) at $R > 0.1$pc around $\sim 10^8 M_\odot$ SMBHs.

Before we consider feedback from the stellar radiative luminosity, which can be a complicated function of stellar mass $M_\star$ and/or radius $R_\star$, the stars' nominal Bondi accretion rate in this environment is given by

$$\dot{M}_{\rm Bondi} = 4\pi R_B^2 \rho_c c_{\rm s,gas} = 4\pi\rho_c \frac{G^2 M_\star^2}{c_{\rm s,gas}^3} \tag{7}$$

where $\Omega = \sqrt{GM_\bullet/R^3} = 2.22\times 10^{-10} m_8^{1/2} r_{\rm pc}^{3/2} s^{-1}$ and $R_B = GM_\star/c_{\rm s,gas}^2$ is the conventional Bondi radius. A point that we would like to clarify is that the sound speed governing Bondi radius, or the critical radius of infall (even without feedback), should be the gas sound speed rather than the radiation sound speed as assumed by Cantiello et al. (2021); Dittmann et al. (2021); Fabj et al. (2025). This is because the density in these regions is not sufficient for the diffusion timescale to be short enough and for radiation to completely couple with the gas, therefore radiation force can act as reduction in further providing feedback (Chen et al. 2024, 2025). From

Eqs. (4), (6), and (7), we find

$$\dot{M}_{\rm Bondi} = 5\times10^{21}\frac{m_8^{3/8}m_\star^2\epsilon_{\bullet 06}^{1/4}}{\lambda_{\bullet 6}^{1/4}r_{\rm pc}^{33/8}}\frac{\rm g}{\rm s} \tag{8}$$

where $m_\star = M_\star/M_\odot$. In the alternative adiabatic regime where the Bondi radius is defined by the combined pressure of radiation and gas, there should not be radiative feedback altogether (Chen et al. 2024).

In the fast-diffusion regime, the diffusive radiation luminosity at the critical radius of infall is responsible for determining the strength of feedback. Simulations show that once an accretion flow with $\dot{M}_{\rm acc}$ is established, in addition to the stars' intrinsic luminosity $L_\star$, both thermal and kinetic energy are released as extra radiation with the accreting mass $\dot{M}_{\rm acc}$ (Chen et al. 2024)

$$L_{\rm acc,th}(\dot{M}_{\rm acc}) = \dot{M}_{\rm acc}c_{\rm s,rad}^2 = \dot{M}_{\rm acc}\frac{aT_c^4}{3\rho_c} \tag{9}$$

$$L_{\rm acc,KE}(\dot{M}_{\rm acc}) = \dot{M}_{\rm acc}V_\star^2 \simeq \dot{M}_{\rm acc}\frac{GM_\star}{R_\star} \tag{10}$$

where $V_\star \simeq \sqrt{GM_\star/R_\star}$ is approximately the Keplerian speed at the stellar surface. Since $V_\star \gg c_{\rm s,rad}$, the advection of thermal energy of the disk gas is generally negligible compared to the advection of gravitational potential energy. This is analogous to the Eddington luminosity for black hole accretion.

With an uninterrupted accretion rate $\dot{M}_{\rm acc} \approx \dot{M}_B$, we can estimate that

$$L_{\rm acc,th} = 0.2m_8^{25/24}\frac{\alpha Q^{5/8}}{(\epsilon/\lambda)^{5/12}}\frac{m_\star^2 L_\odot}{r_{\rm pc}^{15/8}} \tag{11}$$

$$L_{\rm acc,KE} = 200(\epsilon/\lambda)^{1/4}\frac{\alpha Q^{5/8}}{r_{\rm pc}^{15/8}}\frac{m_\star^3}{r_\star}L_\odot \tag{12}$$

where $r_\star = R_\star/R_\odot \simeq m_\star^{0.6}$. Comparing the dominant gravitational term with the stellar Eddington luminosity:

$$L_{{\rm Edd},\star} = 4\pi GM_\star c/\kappa_e = 3.2\times10^4 m_\star L_\odot, \tag{13}$$

where κ_e is the electron scattering opacity, we find $L_{\rm acc,KE} > L_{{\rm Edd},\star}$ when $M_\star \gtrsim 10M_\odot$, which is when the accretion luminosity can provide strong feedback to reduce the accretion rate $\dot{M}_{\rm acc}$ to constrain $L_{\rm acc,KE}(\dot{M}_{\rm acc}) \lesssim L_{{\rm Edd},\star}$.

2.2. *Detailed modeling of radiative feedback*

When the star itself also contributes an intrinsic luminosity $L_\star$, the situation is more complex than the simple estimates given above. In the Bondi regime, $L_\star$ alone will be able to effectively reduce the gravity felt by the ambient gas by a factor

$$\lambda_\star \equiv L_\star/L_{{\rm Edd},\star} = 3\times10^{-5}/\Upsilon, \tag{14}$$

where the mass to light ratio Υ (normalized to its solar value) is a decreasing function of $m_\star$. The critical or effective Bondi inflow rate becomes $(1-\lambda_\star)^2\dot{M}_B$. As $\lambda_\star \to 1$ with $M_\star \to 100M_\odot$, there is a smooth transition toward the Eddington dominated regime such that the accretion rate is capped by the energy limit $L_{\rm acc,KE} + L_{\rm acc,th} \lesssim L_{{\rm Edd},\star} - L_\star = (1-\lambda_\star)L_{{\rm Edd},\star}$ (Chen et al. 2024). Nevertheless, $\dot{M}_{\rm acc}$ should not be completely quenched so that $M_\star$ and $L_\star$ continue to increase.

Formally, Chen et al. (2024) proposes a prescription for $\dot{M}_{\rm acc}$ across all regimes that can be approximated as:

$$\dot{M}_{\rm acc,formal}(\lambda_\star) \approx \min\begin{cases}(1-\lambda_\star)^2\,\dot{M}_{\rm Bondi}\\(1-\lambda_\star)\,\dot{M}_{\rm Edd,KE}\\(1-\lambda_\star)\,\dot{M}_{\rm Edd,th}\end{cases} \tag{15}$$

with

$$\begin{aligned}\dot{M}_{\rm Edd,th} &= \frac{L_{{\rm Edd},\star}}{c_s^2} = \frac{L_{{\rm Edd},\star}3\rho_c}{aT_c^4}\\ &= 6.3\times10^{27}\left(\frac{\epsilon_{\bullet 06}}{m_8\lambda_{\bullet 6}}\right)^{1/3} m_\star\frac{\rm g}{\rm s}\end{aligned} \tag{16}$$

, and

$$\dot{M}_{\rm Edd,KE} = \frac{L_{{\rm Edd},\star}}{V_\star^2} = \frac{L_{{\rm Edd},\star}R_\star}{GM_\star} = 6\times10^{22}r_\star\frac{\rm g}{\rm s}, \tag{17}$$

When the stellar luminosity contributes significantly to the radiative feedback process ($\lambda_\star \sim 1$), the accretion rate $\dot{M}_{\rm acc,formal}$ (Eq. 15) is mostly limited by $\dot{M}_{\rm Edd,KE}$ (Eq. 17) with a characteristic timescale

$$\tau_{\rm Edd,KE} = \frac{M_\star}{\dot{M}_{\rm Edd,KE}} = \frac{\tau_{\rm Sal}R_{\bullet,\star}}{R_\star} \simeq 10^3 m_\star^{0.4}{\rm yr} \tag{18}$$

where $\tau_{\rm Sal} = M_\star c^2/L_{{\rm Edd},\star} = c\sigma/4\pi G m_p = 4.5\times10^8$yr is the Salpeter timescale and $R_{\bullet\star}$ is the star's gravitational radius. For a solar-type star, $\tau_{\rm Edd,KE} \simeq 10^3$ yr and it is about an order of magnitude longer for stars with $M_\star \gtrsim 10^2 M_\odot$.

In practice, the stiffness of $\dot{M}_{\rm acc,formal}$ in Eq. (15) introduces numerical instabilities. We introduce a logistic tapering function:

$$\begin{aligned}S_{\lambda_0}(\lambda_\star) &= \left[\frac{1}{2}\left(1-\tanh(4\ln\frac{\lambda_\star}{\lambda_0})\right)\right]^\beta\\ &= \left[1-\frac{(\lambda_\star/\lambda_0)^8}{1+(\lambda_\star/\lambda_0)^8}\right]^\beta\end{aligned} \tag{19}$$

where λ_0 is the feedback-transition parameter and the power indices β (default 2) is chosen to adjust the sharpness of the transition and to preserve numerical stability. The suppression factor $S_{\lambda_0} \to 1$ for $\lambda_\star \ll \lambda_0$ and $S_{\lambda_0} \to 0$ for $\lambda_\star \gg \lambda_0$. For $\lambda_\star = \lambda_0$, $S_{\lambda_0} = 2^{-\beta}$ with a smooth $d\ln S/d\ln\lambda_\star \propto \lambda_0^{-1}$ transition gradient. The radiative feedback is taken into account with

$$\dot{M}_{\rm acc}(\lambda_\star) = \min \begin{cases} (1-\lambda_\star)^2 \dot{M}_{\rm Bondi} \\ S_{\lambda_0}(\lambda_\star)\dot{M}_{\rm Edd,KE} \\ S_{\lambda_0}(\lambda_\star)\dot{M}_{\rm Edd,th} \end{cases} \tag{20}$$

2.3. *Stellar wind mass loss*

Low-mass stars have momentum dominated, line-driven winds (Lamers & Cassinelli 1999). As $L_{\rm total} \to L_{\rm Edd,\star}$, opacity due to electron scattering provides a much more effective coupling between the radiation and matter than line opacity and can drive energy dominated winds (Owocki & Shaviv 2012).

Under the assumption that a fraction of

$$L_{\rm total} = L_\star + L_{\rm acc,th} + L_{\rm acc,KE} \tag{21}$$

is carried by the energy-dominated wind, we prescribe:

$$\begin{aligned} \dot{M}_{\rm wind} &= (1-S_{\lambda_0})\frac{(L_\star + L_{\rm acc,KE} + L_{\rm acc,th})}{V_{\rm escape}^2} \\ &= (1-S_{\lambda_0})\frac{(L_\star + L_{\rm acc,KE} + L_{\rm acc,th})R_\star}{2GM_\star} \end{aligned} \tag{22}$$

where we used $1 - S_{\lambda_0}$ as a coefficient that transitions from 0 toward 1 smoothly and $V_{\rm escape}^2 = 2GM_\star/R_\star$. The mass loss intensifies and accretion tapers down as $\lambda_\star \to 1$.

Note that it is possible for merging stars to significantly increase their $L_\star$ such that $\lambda_\star \gg 1$ within a few dynamical timescales. In this limit, $S_{\lambda_0} \simeq 0$ and the wind is launched with full intensity $\dot{M}_{\rm wind}$ (Eq. 22) on a time scale

$$\tau_{\rm wind} = M_\star/\dot{M}_{\rm wind} \simeq \tau_{\rm Sal} R_{\bullet,\star}/2\lambda_\star R_\star = \tau_{\rm Edd,KE}/2\lambda_\star \tag{23}$$

comparable to the disk's dynamical timescale $\tau_{\rm dyn} = \Omega^{-1} = 1.5 \times 10^3 m_8^{-1/2} r_{\rm pc}^{3/2}$ yr.

2.4. *Quasi accretion–wind equilibrium*

Taking both accretion and wind into account, the stellar mass evolves with a net rate

$$\dot{M}_{\rm net} = \dot{M}_{\rm acc} - \dot{M}_{\rm wind}. \tag{24}$$

When a quasi accretion–wind equilibrium in which $\dot{M}_{\rm acc} = \dot{M}_{\rm wind}$ is established with $\lambda_\star = \lambda_{\rm equi}$, $S_\lambda \dot{M}_{\rm Edd,KE}$ usually sets the limit on $\dot{M}_{\rm acc}$ in Eq. (20). Combining with Eq. (10) Eq. (17) and (22), we find

$$2S_{\lambda_0} = (1-S_{\lambda_0})(\lambda_\star + S_{\lambda_0}). \tag{25}$$

From Eqs. (19) and (25), we can determine the equilibrium $\lambda_\star \simeq \lambda_{\rm equi} \simeq \lambda_0$ due to the tapering form of S_{λ_0}. The evolution tracks for immortal stars of any initial mass are expected to converge to this state, while metamorphic stars will eventually deviate due to exhaustion of hydrogen.

3. METHODOLOGY

We study stellar evolution in AGN–disk conditions using the one-dimensional code `MESA` (Paxton et al. 2011, 2013, 2015, 2019; Jermyn et al. 2023), building on the public package of Cantiello et al. (2021) and Jermyn et al. (2021). Here, we outline some details of the simulation setup, including modifications for AGN–disk accretion, wind-loss, chemical mixing, as well as our explored parameter space.

3.1. *Code Setup and Initial Conditions*

Stars are evolved with `MESA`v22.11.1. We employ a nuclear network `approx21` capable of tracking the main sequence and post–main–sequence evolution up to the onset of silicon burning. Calculation is terminated when MESA encounters numerical issues just before stellar collapse. Strict resolution controls are imposed to ensure stability during rapid mass change. `MESA` uses radiative opacities from OPAL (Iglesias & Rogers 1996), supplemented at low temperatures by Ferguson et al. (2005) and at high temperatures by Poutanen (2017), with electron conduction opacities from Cassisi et al. (2007); Blouin et al. (2020). Nuclear reaction rates combine JINA, REACLIB and NACRE with additional weak rates (Cyburt et al. 2010; Angulo et al. 1999; Fuller et al. 1985; Oda et al. 1994), include screening Chugunov et al. (2007), and adopt neutrino losses from Itoh et al. (1996).

3.2. *Model Parameters and Boundary Conditions*

At the onset of each calculation, the zero-age main-sequence (ZAMS) star has $M_\star = M_\odot$ and $Z = Z_\odot$. The stellar surface pressure and temperature are set to be those of the local disk mid-plane. Our model parameters (Table 1) span $\rho_{\rm c} = 10^{-17}$–10^{-13} g cm^{-3}, $c_{\rm s,gas} \approx 10^6$ cm s^{-1}, and $T_{\rm c} \simeq 10^5$ K (Eq. 5). These values are appropriate for various radii around SMBH with different masses (§2.1).

For the abundances of the accreted disk gas, we explore $Y_{\rm d} = 0.25$–0.7, $Z_{\rm d,C} = 2.2 \times 10^{-3}$, $Z_{\rm d,N} = 7 \times 10^{-4}$, and $Z_{\rm d,O} = 6.3 \times 10^{-3}$ for C, N, and O respectively.

Table 1. Model Parameters and Resulting Masses

λ_0	Y_d	ρ_c [a]	M_max	M_Hdep [b]	$\log \tilde{L}_{1+2}$ [d]	$\log \tilde{L}_2$ [e]
			Standard Mixing [c]			
0.25	0.25	10^{-16}	58.80	6.81	5.074	5.292
0.50	0.25	10^{-16}	122.1	10.46	5.276	5.810
0.75	0.25	10^{-16}	234.3	14.75	5.649	6.113
0.90	0.25	10^{-16}	337.9	17.58	5.730	6.262
0.50	0.25	$\mathbf{10^{-17}}$	82.48	9.83	4.725	5.529
0.50	0.25	$\mathbf{10^{-16}}$	122.1	10.46	5.276	5.810
0.50	0.25	$\mathbf{10^{-15}}$	132.9	12.33	5.449	5.772
0.50	0.25	$\mathbf{10^{-14}}$	128.8	13.66	5.505	5.771
0.50	0.25	$\mathbf{10^{-13}}$	127.1	14.05	5.510	5.774
0.75	**0.30**	10^{-16}	186.4	14.20	5.619	6.020
0.75	**0.40**	10^{-16}	132.8	14.53	5.608	5.938
0.75	**0.50**	10^{-16}	94.40	14.46	5.557	5.866
0.75	**0.60**	10^{-16}	63.97	14.65	5.457	5.762
0.75	**0.70**	10^{-16}	40.02	14.80	5.317	5.632
			Extra Mixing [c]			
0.50	0.25	10^{-16}	122.18	···	···	6.246
0.75	0.25	10^{-16}	234.28	···	···	6.666
0.90	0.25	10^{-16}	337.98	···	···	6.875

NOTE—a

Units: ρ_c in $\mathrm{g\,cm^{-3}}$; masses in $M_\odot$; luminosities in $\log_{10}(L/L_\odot)$.

NOTE—b

M_max is the peak mass; M_Hdep is the mass at central H–depletion (standard-mixing models only).

NOTE—c

"Standard mixing" uses $D_\mathrm{mix,rad} = 10^5\ \mathrm{cm^2\,s^{-1}}$; "Extra mixing" as described in §3.4.

NOTE—d

$\log \tilde{L}_{1+2}$: average luminosity from model start to central-H depletion (or to the last model if H–depletion is not reached).

NOTE—e

$\log \tilde{L}_2$: average luminosity from peak mass to TAMS/the last model.

3.3. *Accretion and Wind-loss Implementation*

At every timestep, we separately compute the accretion and continuum-driven wind rates, taking into account radiative-feedback with $\beta = 2$ [1], $\lambda_0 = 0.25$–0.90 in the tapering function S_{λ_0} (Eq. 19). With $S_{\lambda_0} \to 0$ as $\lambda_\star \to 1$, super-Eddington inflow is quenched.

Accretion and wind occur concurrently with the same S_{λ_0}. Wind loss is implemented first with $\dot{M}_\mathrm{wind}$ from Eq. (22). For $|\dot{M}_\mathrm{wind}|\Delta t$ smaller than the outermost cell mass, gas in the surface cell is removed entirely; the excess fraction is then the replenishment of the excess fraction with a fixed composition of the circumstellar gas. If the amount to be removed exceeds the surface cell, successive outer cells are stripped until the total removed mass matches $|\dot{M}_\mathrm{wind}|\Delta t$.

Treatment of the wind loss is followed by applying accretion ($\dot{M}_\mathrm{acc}$) to the exposed layers using the composition of the circumstellar gas. This sequence leads to $\dot{M}_\mathrm{net}$ in accordance with Eq. (24). Typical net mass loss rates stay within $10^{-12} - 10^{-4} M_\odot \mathrm{yr}^{-1}$, enforced by a timestep cap of $\Delta t \leq 10^{10}$ s to preserve numerical stability throughout the post-main–sequence phase.

The star–disk mass exchange may modify the abundance of the circumstellar gas. In most models, we assume total decoupling between the accretion flow and the outgoing wind, meaning that accreted gas carries the same composition as the disk initial condition. We also briefly consider the possibility of total retention (Ali-Dib & Lin 2023), i.e., the stars accrete *in situ* the gas polluted by their own wind in §4.6.

3.4. *Chemical Mixing Diffusivity*

Along the evolutionary tracks, stars contain both radiative and convective zones. We use the default mixing length prescription in `MESA` for convective zones. The metamorphic stellar models are generated by setting a uniform level for minimal diffusivity $D_\mathrm{mix,rad} = 10^5\,\mathrm{cm^2\,s^{-1}}$ for the radiative envelopes, similar to other standard `MESA` models, including Xu (2025, in press). The immortal stars are constructed with an *ad hoc* "extra- mixing" prescription, in which $D_\mathrm{mix}(r)$ is assumed to increase with stellar radiative flux F (Cantiello et al. 2021).

4. RESULTS

4.1. *Initial Growth: Dependence on λ_0 and ρ_c*

Below we present the outcomes of our `MESA` calculations over a range of model parameters (Table 1), and derive various quantities from these simulations.

Figure 2 shows the evolution of stellar mass as a function of time, for several sets of representative models. During the initial evolution, $L_\mathrm{total} < L_{\star,\mathrm{Edd}}$ (Eqs. 13 & 21) such that $S_{\lambda_0} \sim 1$, $\dot{M}_\mathrm{acc} \gg \dot{M}_\mathrm{wind}$ (Eqs. 19, 20, & 22), and the stellar mass $M_\star$ undergo runaway growth, with a rate $\dot{M}_\mathrm{acc} \sim \dot{M}_\mathrm{Edd,KE}$ (Eq. 20) which is *independent* of ρ_c (Eq. 17). Panel b in Fig. 2 shows that $M_\star$ ($\gtrsim 10 M_\odot$) grows at similar rates across most ($R \lesssim$ a few pc) regions of the disk.

The radiation feedback becomes strong enough to suppress accretion to intensify mass loss through stellar wind with $\lambda_\star \to \lambda_0$ and $S_{\lambda_0} < 1$ as $M_\star$ reaches above a

[1] we tested $\beta = 1, 3$ and the results are not sensitive to this hyper-parameter.

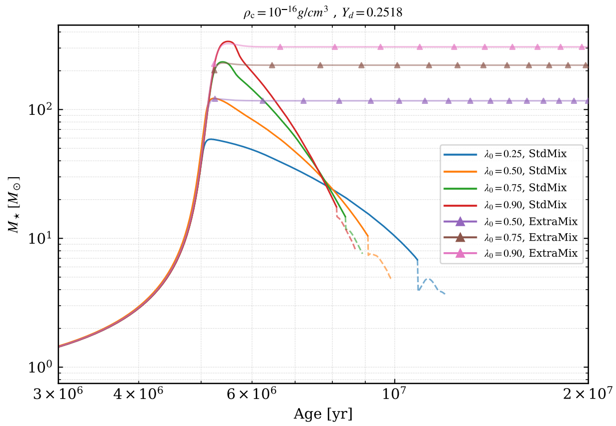

(a) Mass evolution for different λ_0

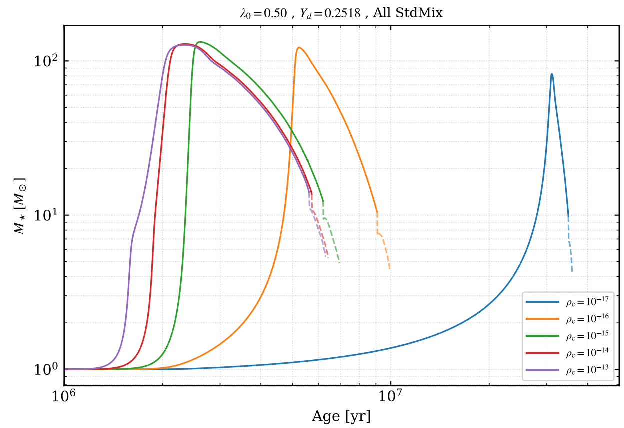

(b) Mass evolution for different ρ_c

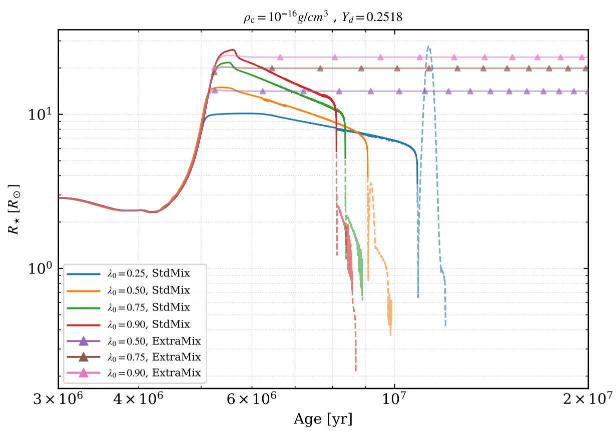

(c) Radius evolution for different λ_0

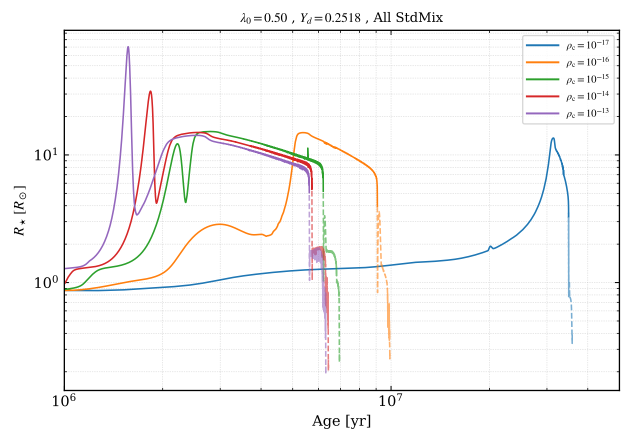

(d) Radius evolution for different ρ_c

Figure 2. Evolution of stellar mass (top row) and radius (bottom row). Panels (a) and (c) compare different feedback-suppression parameters λ_0 at fixed mid-plane density $\rho_c = 10^{-16}\,\mathrm{g\,cm^{-3}}$, while panels (b) and (d) compare different densities at fixed $\lambda_0 = 0.5$. Solid curves show the standard mixing models; Triangular markers in panels (a) and (c) denote models with radiative-flux–induced "extra" mixing, of which the main-sequence phase persists indefinitely. The semi-transparent curves trace the post–main-sequence evolution. As $\lambda_0 \to 1$, feedback suppression weakens, yielding rapid mass growth followed by moderate mass loss; conversely, as $\lambda_0 \to 0$, strong suppression enforces more moderate mass growth. Panels (b) and (d) show ambient density plays a minor role from $\rho_c \sim 10^{-17}$ g cm^{-3} to $\rho_c \sim 10^{-13}$g cm^{-3}, (typical of the innermost AGN disk), our feedback prescription successfully limits runaway accretion; the disk helium mass fraction is set to $Y_\mathrm{d} = 0.25$.

few tens $M_\odot$. This transition marks the onset of an accretion–wind equilibrium (with $\dot{M}_\mathrm{acc} \simeq \dot{M}_\mathrm{wind}$), which limits the star's initial growth rate with a maximum $M_\star = M_\mathrm{max}$ with $\lambda_\star \simeq \lambda_0$ (Eq. 25).

In general, $L_\star$ and $\lambda_\star$ are functions of $M_\star$ and $Y_\star$ (Owocki & Shaviv 2012), such that the value of λ_0 can be used to infer a stellar mass $M_\star = M_\mathrm{equi}(\lambda_0, Y_\star)$ for quasi accretion–wind equilibrium as a function of the time-dependent helium abundance $Y_\star$, see § 4.3. During the initial accretion phase, $Y_\star \sim Y_d$ so that M_max depends on both λ_0 and Y_d (panel a, Figs. 2 & 4). After reaching M_max, the evolution tracks of immortal and metamorphic stars begin to dramatically diverge.

4.2. *Subsequent Evolution of Immortal vs. metamorphic stars: Dependence on Mixing*

In models with extra mixing imposed in the radiative zone (triangular symbols), the star attains an asymptotic mass M_IMS with a slightly sub-Eddington luminosity L_IMS when the accretion and wind rates cancel each other. In the full-retention limit, the circumstellar gas is locally contaminated by the stellar wind to have the same composition as the stellar surface, all stars must be metamorphic due to retention of materials from the stellar wind, *even* with flux-induced extra-mixing (Ali-Dib & Lin 2023).

In this paper, we present most models with zero retention such that the outer mass-exchange region of the star is continually refreshed with the abundance of the disk gas. The outer stellar envelope contains radiative zones which separates the nuclear burning core from the mass exchange region. With "extra mixing", Cantiello et al. (2021) showed the core would be replenished with the H–laden accreted gas and purged its He ashes to indefinitely prolong these "immortal" stars' main–sequence evolution.

An order of magnitude estimate and a series of `MESA` models with various values of $D_{\rm mix,rad}$ suggest that the mixing of a significant fraction of the freshly accreted H–rich gas from the disk with the He ashes in the core can be accomplished over the characteristic H–exhaustion timescale (in the absence of efficient mixing) $\tau_{\rm He} \sim 3$ Myr (Eq. 28 in §4.3 below) provided $D_{\rm mix,rad} \gtrsim \Delta R^2/\tau_{\rm He} \gtrsim 10^{11}$ cm^2 s^{-1} where ΔR is the radial extent of the radiative layer (Xu, 2025, in press). This required value of $D_{\rm mix,rad}$ is much larger than its typical value estimated for rotation-induced shear mixing implied in (Prat & Lignières 2014; Maeder & Meynet 2010; Spruit 2002) and prescribed in the conventional `MESA` models. This calculation implies that most AGN-embedded stars should be chemically stratified once they reach accretion–wind equilibrium and are likely to evolve off the main sequence as "metamorphic" stars, despite ongoing zero-retention mass-exchange with the disk.

For models with the standard mixing prescription and various values of λ_0 and $Y_{\rm d}$, the stellar mass reaches maximum values $M_{\rm max}$ similar to immortal stars with corresponding model parameters. However, with an inadequate H diffusion and replenishment to the core (even for our assumption of zero-retention of stellar wind materials), quasi accretion–wind equilibrium is maintained with an increasing $Y_\star$ and decreasing $M_\star$. Details of this phase is elaborated in §4.3 where we discuss models with different Y_d to aid our analysis.

After exhausting H in the convective core, the star undergoes He burning through triple-α process and undergoes a transition to post main–sequence evolution. The doubling of its luminosity (above $L_{\rm Edd,\star}$) leads to fractional reduction of its mass with a modest expansion of its radius (Fig. 2). This transition of the metamorphic stars in AGN disk is in contrast to the red-giant phase of stand-alone stars in the Galaxy. An exception is the $\lambda_0 = 0.25$ (strong-feedback) model which produced a red-giant expansion followed by a $R_\star$ contraction after the onset of He burning. Finally, the depletion of He leads to the nuclear burning of other elements until the star undergo core-collapse, leaving behind a black hole of mass perhaps $5 \sim 15\,M_\odot$, with or without type II supernova (Fryer et al. 2025).

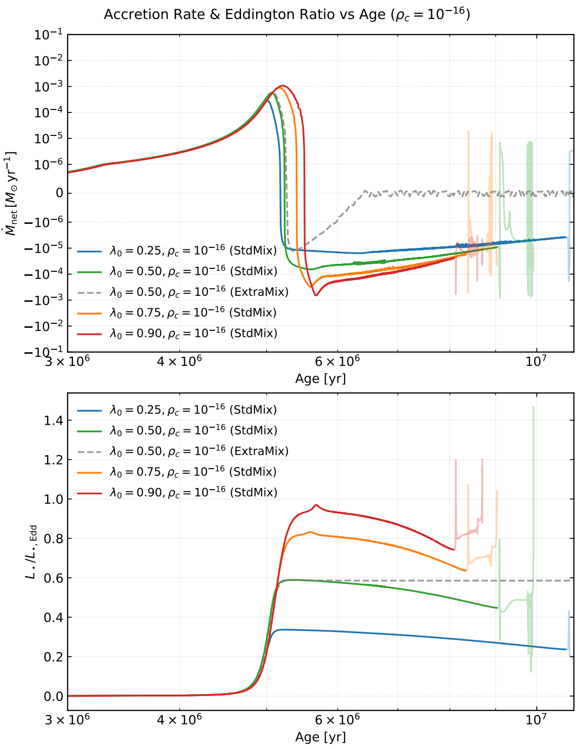

Figure 3. Evolution of net mass-exchange rate $\dot{M}_{\rm net}$, i.e. the accretion rate deducts the absolute value of the wind-loss rate is shown in the upper panel. The Eddington ratio $L_\star/L_{\rm Edd,\star}$ is shown in the lower panel for the fiducial model with $\rho_c = 10^{-16}\,{\rm g\,cm^{-3}}$, $Y_{\rm d} = 0.25$, and various values of λ_0. Opaque curves indicate main–sequence and partially transparent curves represent post-main–sequence phases after core hydrogen exhaustion. The dashed line represents the immortal-star model with $\lambda_0 = 0.5$ and extra mixing.

Figure 3 illustrates the time evolution of $\dot{M}_{\rm net}$ and $\lambda_\star$ for models with a fixed $\rho_c = 10^{-16}$g/cm^3, highlighting the difference between immortal and metamorphic stars. During the first $\sim$5 Myr, $\dot{M}_{\rm acc}$ ramps up to its maximum (on the order of $10^{-4} - 10^{-3} M_\odot$/yr). Since $L_\star < \lambda_0 L_{\rm Edd,\star}$, $\dot{M}_{\rm wind}$ is negligible during this growth phase. The Eddington ratio $\lambda_\star$ rises as the $M_\star$ grows (Eq. 14). At $t \approx 5$ Myr, $\lambda_\star \to \lambda_0$ and radiative feedback begins to quench $\dot{M}_{\rm acc}$ and $\dot{M}_{\rm net}$ decreases precipitously after 5 Myr. For metamorphic stars, $\dot{M}_{\rm net}$ becomes negative during this He-enriching main–sequence phase. For the immortal star example ($\lambda_0 = 0.5$) shown in Figure 3, the net mass loss reduces to zero due to continuous exchange of composition with the disk background and both $M_\star$ and $\lambda_\star$ are maintained at constant values.

4.3. *Evolution of equilibrium mass: Effect of Y_d and $Y_\star$*

Figure 4 shows the evolution track for different helium environmental abundance. A very clear trend is that the

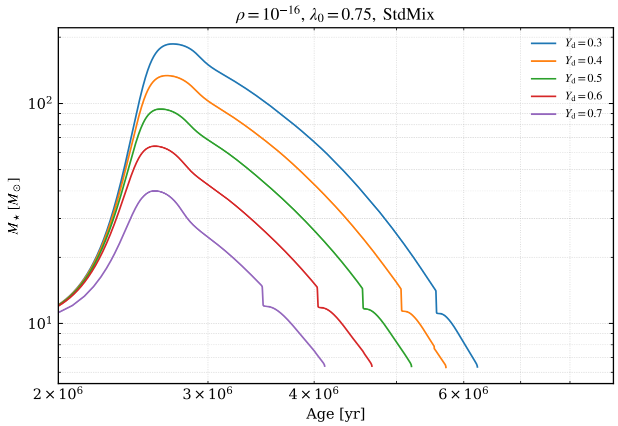

(a) Stellar mass $M_\star$ evolution for different disk helium-fractionY_d

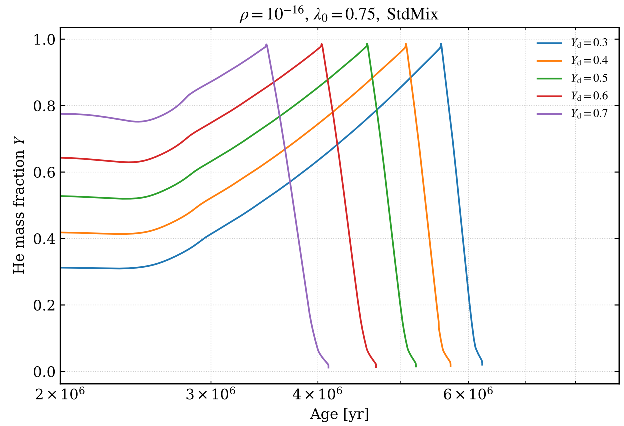

(b) Stellar helium-fraction $Y_\star$ evolution for different disk helium-fraction Y_d

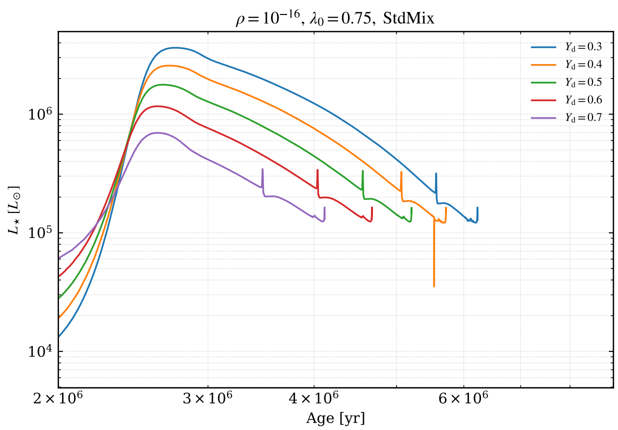

(c) Luminosity evolution for different Y_d

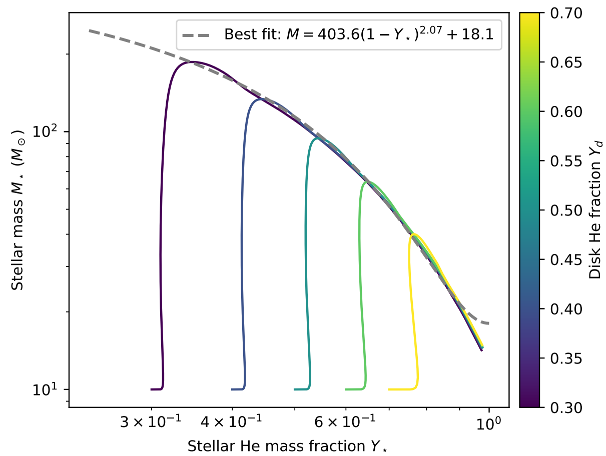

(d) Stellar $Y_\star$ vs $M_\star$ relation with power-law fit

Figure 4. Stellar evolutionary tracks for varying disk helium mass fractions $Y_{\rm d} = 0.3$–0.7, with fixed $\rho_{\rm AGN} = 10^{-16}{\rm g\,cm^{-3}}$ and $\lambda_0 = 0.75$. Panels show the evolution of (a) stellar mass $M_\star$, (b) helium mass fraction $Y_\star$, (c) luminosity $\log L_\star$, and (d) the $Y_\star$–$M_\star$ relation during main–sequence evolution. As $Y_{\rm d}$ increases, higher mean molecular reduces the mass-to-light ratio Υ, causing stars to reach the feedback limit with lower final masses. Panel (d) shows the best-fit power-law relation (grey dashed) between $Y_\star$ and $M_\star$ during equilibrium growth, as predicted by Eq. (31). Because models start from $10M_\odot$, the ramp-up time is shortened.

overall mass scales down with Y_d, offering insight into the mechanism driving quasi-steady mass loss following the initial growth phase. Since $\tau_{\rm acc,KE} \ll \tau_{\rm He}$ (Eqs. 18 and 28), the helium fraction in the star $Y_\star \sim Y_d$ when the stars have just reached their maximum mass (lower right panel). Due to the dependence of stars (or more generally stellar population's) mass-to-light ratio $\Upsilon(M_\star, Y_\star)$ on the average molecular weight(Owocki & Shaviv 2012; Ali-Dib & Lin 2023), the maximum mass at initial equilibrium $M_{\rm max}(\lambda_0, Y_d) \simeq M_{\rm equi}(\lambda_0, Y_\star \simeq Y_d)$ for a given λ_0 scales down with $Y_{\rm d}$ (or equivalently, up with $X_{\rm d}$).

After this point, $Y_\star$ and the average molecular weight increase with time. Since $\Upsilon(M_\star, Y_\star)$ is a decreasing function of $M_\star$ and $Y_\star$, the preservation of the quasi accretion–wind equilibrium with $\lambda_\star \sim \lambda_0$ (Eq. 25) and

$$\Upsilon_{\rm equi} = 3 \times 10^{-5}/\lambda_0, \tag{26}$$

from Eq. (14), requires $M_\star$ to decrease with increases in $Y_\star$ (Fig. 3 in Ali-Dib & Lin (2023)) on the hydrogen depletion timescale $\tau_{\rm He}$ (Eq. 28) in the nuclear burning core, regardless the initial helium contents. Moreover, $L_\star$ of massive stars increases with $M_\star$ slightly steeper than a linear relation so their Υ decreases slowly with $M_\star$ and small changes in λ_0 and $\Upsilon_{\rm equi}$ (Eq. 26) lead to notable modification to the equilibrium mass $M_{\rm equi}$.

To model the time-dependence of stellar mass in this quasi-steady mass loss phase, we may assume $\lambda_\star \sim \lambda_0$

and write the energy equation as

$$\epsilon_{\rm He}\dot{M}_{\rm H}c^2 \simeq \lambda_0 L_{\rm Edd,\star} \tag{27}$$

where $\dot{M}_{\rm H}$ is the hydrogen consumption rate and $\epsilon_{\rm He} \sim 0.007$ is the conversion efficiency from rest-mass energy into radiation. In the CNO cycle on the main sequence, He is enriched at the same rate as H is depleted, i.e. $\dot{M}_{\rm He} = \dot{M}_{\rm H}$ and $\dot{Y}_\star = -\dot{X}_\star$. The characteristic timescale for H depletion (or equivalently He enrichment) in the nuclear burning core (with a mass $M_{\rm core} \lesssim M_\star$) is

$$\tau_{\rm He} \simeq \frac{X_\star M_{\rm core}}{\dot{M}_{\rm H}} \simeq \frac{X_\star \epsilon_{\rm He}\tau_{\rm Sal}}{\lambda_0}\frac{M_{\rm core}}{M_\star} \sim 3\frac{X_\star M_{\rm core}}{\lambda_0 M_\star}{\rm Myr} \tag{28}$$

where $\tau_{\rm Sal} \simeq M_\star c^2/L_{\rm Edd,\star}$ is the Salpeter timescale.

In massive stars, most of the mass is contained in the convective core, i.e. $M_{\rm core} \sim M_\star$ so that the normalized enrichment rate becomes

$$\dot{Y}_\star = \frac{\dot{M}_{\rm H}}{M_\star} \simeq \frac{\lambda_0}{\epsilon_{\rm He}\tau_{\rm Sal}} \tag{29}$$

which leads to a linear increase of $Y_\star$ (with a universal slope independent of the value of initial Y_d, lower right panel) with duration of time after reaching maximum mass at t_0:

$$Y_\star \simeq Y_d + \frac{\lambda_0(t-t_0)}{\epsilon_{\rm He}\tau_{\rm Sal}}, \tag{30}$$

Since $\tau_{\rm He} \gg \tau_{\rm acc,KE}$ and $\tau_{\rm He} \gg \tau_{\rm wind}$ (Eqs. 18 and 23), a quasi-steady mass loss state is maintained. As $Y_\star$ increases with He enrichment, $M_\star(Y_\star)$ converging to the intrinsic values of $M_{\rm equi}(\lambda_0, Y_\star)$. For a given λ_0, the results of the `MESA` models can be fitted (Bottom right panel in Fig. 4) as

$$M_{\rm equi}(\lambda_0, Y_\star) \simeq M_{\star,\rm H}(\lambda_0)(1-Y_\star)^2 + M_{\star,\rm He}(\lambda_0) \tag{31}$$

where $M_{\star,\rm H}(\lambda_0)$ and $M_{\star,\rm He}(\lambda_0)$ are numerical values that can be interpreted as the mass of a fully hydrogen and fully helium star at Eddington ratio λ_0. This fit satisfies both $\lambda_\star \simeq \lambda_0$, and the stellar mass-to-light $\Upsilon(M_\star, Y_\star) = \Upsilon_{\rm equi}$ (Eq. 26) relation. From Bottom right panel in Fig. 4, we can fit $M_{\star,\rm H} \sim 400M_\odot$ and $M_{\star,\rm He} \sim 18M_\odot$ for $\lambda_0 = 0.75$, so the mass *time-dependence* after t_0 can be described by

$$\begin{aligned} M_\star &= M_{\rm equi}(\lambda_0, Y_d, t-t_0) \\ &\simeq M_{\star,\rm H}(\lambda_0) + M_{\star,\rm He}(\lambda_0)\left(1 - Y_d - \frac{\lambda_0(t-t_0)}{\epsilon_{\rm He}\tau_{\rm Sal}}\right)^2 \end{aligned} \tag{32}$$

When H in their core is exhausted (with $Y_\star \to 1$), stars undergo transition to post-main–sequence with a $M_\star$ which is greatly reduced from its maximum values shortly after their formation. For $\lambda_0 \sim 0.5-0.9$, $M_\star$ ranges from $10.5M_\odot - 17.7M_\odot$ at the stage of H exhaustion in the core.

4.4. *Stellar Population*

In contrast to stand-alone stars in the Galaxy, metamorphic stars in AGN disks with the same age $(t-t_0)$ have the same values of $Y_\star$ (Eq. 30), $M_\star(\simeq M_{\rm equi})$ (Eq. 31), $\lambda_\star(\simeq \lambda_0)$, and $L_\star(\simeq \lambda_0 L_{\rm Edd,\star})$. At any given time t, their luminosity and mass functions are determined by their formation epoch t_0.

We partition the evolution into four phases: Phase 1—initial ramp to the maximum mass $M_{\rm max}$ with $\dot{M}_{\rm acc} \gg \dot{M}_{\rm wind}$; Phase 2—$M_{\rm max}$ to central-H depletion; Phase 3—central-H depletion (onset of He burning) to central-He depletion (onset of C burning); Phase 4—central-He depletion (C burning) to pre-collapse (Si burning).

4.4.1. *Luminosity and Energy Output*

During their finite lifespan $\tau_\star(\sim$ a few Myr $\geq \tau_{\rm He})$, metamorphic stars have an average luminosity

$$\tilde{L}_{\rm total} = \frac{1}{\tau_\star}\int_0^{\tau_\star} L_{\rm total}(t)dt, \tag{33}$$

which includes the feedback luminosity from accretion flows (Eq. 21). This quantity is computed from the `MESA` models for a) the entire main sequence, including the initial ramp up to $M_{\rm max}$ ($\tilde{L}_1$ in phase 1); b) the duration of main sequence between $M_\star = M_{\rm max}$ to the terminal age main sequence TAMS with $M_{\rm max} \geq M_\star \geq M_{\rm TAMS}$ ($\tilde{L}_2$ in phase 2); He ignition to depletion ($\tilde{L}_3$ in phase 3); and C ignition to core collapse ($\tilde{L}_4$ in phase 4).

The last two columns in Table 1 indicate that $\tilde{L}_{\rm total}$ in phase 2 ($\tilde{L}_2$) is much larger than that including entire MS (phase 1+2, $\tilde{L}_{1+2}$), especially for relatively small ρ_c. This difference is caused by the slow initial (when $M_\star \sim 1M_\odot$) Bondi accretion. But this difference is modest ($\sim 2-3$) in the high-ρ_c limit, when $\dot{M}_{\rm acc}$ is limited by $\dot{M}_{\rm acc,KE}$ (Eq. 20). In general, $L_{\rm IMS} \gtrsim 2\tilde{L}_2$. Since $\Upsilon(M_\star, Y_\star)$ is a decreasing function of λ_0, $M_{\rm max}$ (with $\Upsilon_{\rm equi}$ in Eq. 26) increases with λ_0, i.e. less efficient feedback generally leads to larger $\tilde{L}_{\rm total}$ and its corresponding average mass. Moreover, $\tilde{L}_2$ is several times larger than that during the post main–sequence evolution ($\tilde{L}_{3+4}$) because a) $M_\star$ has already reduced substantially on the main sequence and b) all metamorphic stars have approximately Eddington-limited luminosity.

4.4.2. *Implication on stellar surface density and formation rate*

In an opaque disk, radiative diffusion leads to a surface cooling rate of

$$\mathcal{Q}^- = \frac{32\sigma T_c^4}{3\kappa\Sigma} = \frac{8c\rho c_{\rm s,rad}^2}{\kappa\Sigma}, \tag{34}$$

Assuming the embedded metamorphic stars have a uniform age distribution and all their luminosity is converted into thermal energy of the disk gas, their heating rate per unit are would be $\mathcal{Q}_\star^+ \simeq s_\star \tilde{L}_{\rm total}$. In a thermal equilibrium ($\mathcal{Q}_\star^+ = \mathcal{Q}^-$), the surface density of stars would be (Chen & Lin 2024)

$$s_\star = \frac{\mathcal{Q}^-}{\tilde{L}_{\rm total}} = \frac{4c}{\kappa}\frac{\Omega c_{\rm s,rad}}{\tilde{L}_{\rm total}}. \tag{35}$$

Since the metamorphic stars are generally less luminous that the immortal stars (Fig. 2), their $\tilde{L}_{\rm total}$ is also less than $L_\star$ of the immortal stars. Consequently, more metamorphic stars than immortal stars are needed to maintain the thermal equilibrium of disks with marginal gravitational stability (with Toomre $Q \simeq 1$).

In a quasi accretion–wind equilibrium with $\lambda_\star \sim \lambda_0$, $\tilde{L}_{\rm total}$ also provide an estimate on the average mass of the star $\tilde{M}_\star \sim M_\odot \tilde{L}_{\rm total}/\lambda_0 L_{\rm Edd,\odot}$. Although the metamorphic stars' average mass is a fraction of its maximum value ($\sim M_{\rm max}(\lambda_0)(1-Y_{\rm d})^2 \sim M_{\rm IMS}$ in Eq. 32), their total mass surface density $s_\star \tilde{M}_\star$ and flux are the same as the immortal stars.

All metamorphic stars loss mass to the disk during their evolution. As they fade, the disk contracts with smaller Q and resumption of gravitational instability and fragmentation (Chen et al. 2023). Over time, the thermal equilibrium of the disk is restored and maintained with the formation of a new generation of metamorphic stars at a rate $\dot{s}_\star \sim s_\star/\tau_\star$.

The newly formed stars' initial growth timescale ($\tau_{\rm acc} = M_\star/\dot{M}_{\rm acc}$; Eq. 20) depends on $\rho_{\rm c}$ (Eq. 7) and $M_\star$ (Eq. 18) which may have an initial range extending to the sub-solar limit. Moreover, $\tau_{\rm Bondi} \gg \tau_{\rm dyn} = \Omega^{-1}$ for low-mass ($M_\star \lesssim 10 M_\odot$) stars (§2.2). This bottleneck leads to an over-production of low-mass stars which subsequently merge and grow much more rapidly than through gas accretion (Wang et al. in prep). In a sufficiently populated stellar system, the mass of all continually forming metamorphic stars can rapidly grow to $\sim M_{\rm max}(\lambda_0)(1-Y_{\rm d})$ and thereafter a quasi-equilibrium can be established in which accretion and wind mass-loss balance ($\dot{M}_{\rm net} \simeq 0$, or $\dot{M}_{\rm acc} \simeq \dot{M}_{\rm wind}$ in Eq. 24). This balance enables self-regulation of the star formation rate in the disk and prevents runaway feedback instabilities.

4.5. *Chemical Yields without Wind Retention*

In this section, we discuss the net elemental yield from both immortal and metamorphic stars to the disk. We integrate the net yield (mass return from star to the disk) for element Z (including C, N, and O separately)

$$\Delta M_{\rm Z} = \int_{\Delta\tau} (\dot{M}_{\rm wind} Z'_\star - \dot{M}_{\rm acc} Z_{\rm d}) dt \tag{36}$$

where $Z'_\star$ is the abundance near the mass losing layer on the stellar surface and $\Delta\tau$ is the time interval for relevant stages of stellar evolution. Note that $Z'_\star$, $\dot{M}_{\rm wind}$, and $\dot{M}_{\rm acc}$ are all functions of $M_\star$. The He return is calculated with a similar expression.

During phase 1, $M_\star$ ramps up with $\dot{M}_{\rm acc} \gg \dot{M}_{\rm wind}$, so that the retention effect is negligible and $\Delta M_{\rm Z} \sim -M_{\rm max} Z_{\rm d}$. But, stellar wind steeply intensifies as $M_\star \sim M_{\rm max}$ with $\lambda_\star \sim \lambda_0$ (§3.3). In this subsection, we consider default models that all the gas released by the stellar wind is completely return to the disk, i.e. without any retention.

4.5.1. *C+O depletion by Immortal stars*

If the freshly-accreted gas can mix with gas in the convective core, the replenishment of H–fuel to would indefinitely prolong the main–sequence evolution and render the stars embedded in AGN disks "immortal". Through the CNO cycle, these stars convert H into He at a rate $\dot{M}_{\rm He} = L_\star(\lambda_0)/\epsilon_{\rm He} c^2$. Concurrently, it also converts C and O into N at a rate of $\dot{M}_{\rm N}$ while the total C+N+O abundance is conserved.

For a representative model with $\lambda_0 = 0.75$ and $\rho_{\rm c} = 10^{-16}$g cm^{-3}, we estimate $\dot{M}_{\rm He} \sim 5\times10^{-5} M_\odot{\rm yr}^{-1}$ and $\dot{M}_{\rm N} \sim 5\times10^{-6} M_\odot{\rm yr}^{-1} \sim 0.1 \dot{M}_{\rm He}$ (bottom-right, panel (f), Fig. 5). Since the fusion byproducts are recycled, the disk is polluted in He and N at rates $\dot{M}_{\rm He}$ and $\dot{M}_{\rm N}$ per star respectively. The conservation of C+N+O also implies that the C+O are depleted at a rate $\sim 0.5\dot{M}_{\rm N}$. Composite quasar spectra and photo-ionization modeling show modest enhancement in He. The median BLR metallicity of $Z \approx 4$–$6\, Z_\odot$ for all α-elements (including C, N, and O) across $2 \lesssim z \lesssim 6$, without a significant redshift evolution (Fig. 6 in Huang et al. (2023)). These spectroscopic data is not consistent with the prolific return of He to and depletion of C and O inferred for the immortal stars.

4.5.2. *Metamorphic stars' Main sequence yields*

In contrast, the radiative layer of metamorphic stars separates their core from the surface region where gas is accreted and return to the disk. As He and N are enhanced with the depletion of H, C, and O, they are well mixed in the core. As these stars loss mass, the boundary between the convective core and radiative envelope rezones. The N-laden gas later exudes into the surface layers and is eventually released into the surrounding disk.

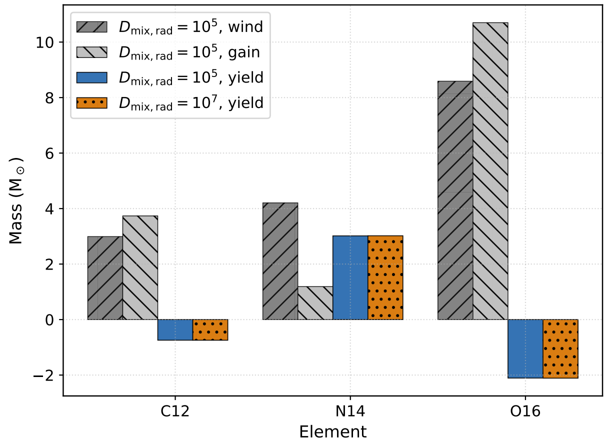

(a) Metamorphic star, CNO yields, init → central H depletion

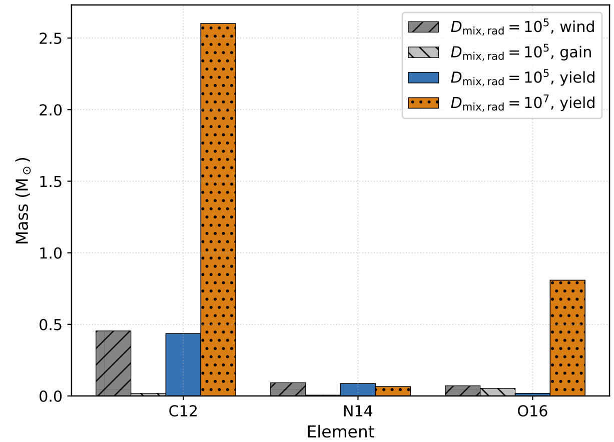

(b) Metamorphic star, CNO yields, central H depletion → central He depletion

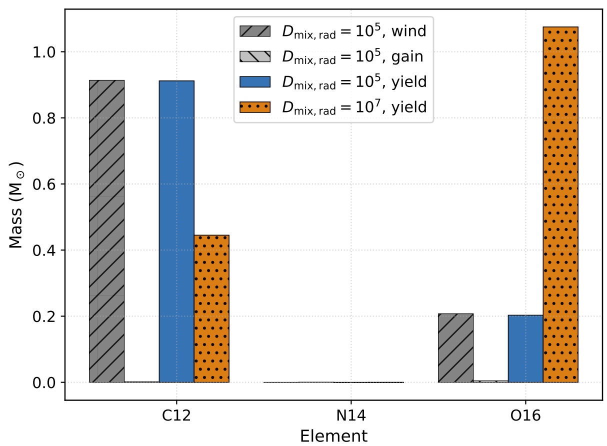

(c) Metamorphic star, CNO yields, central He depletion → pre-collapse

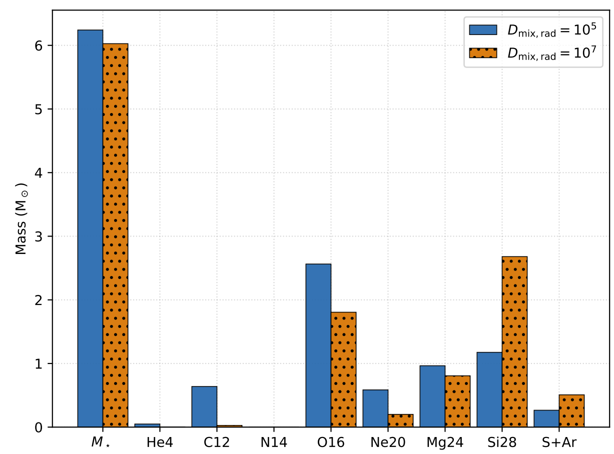

(d) Metamorphic star, pre-collapse composition totals

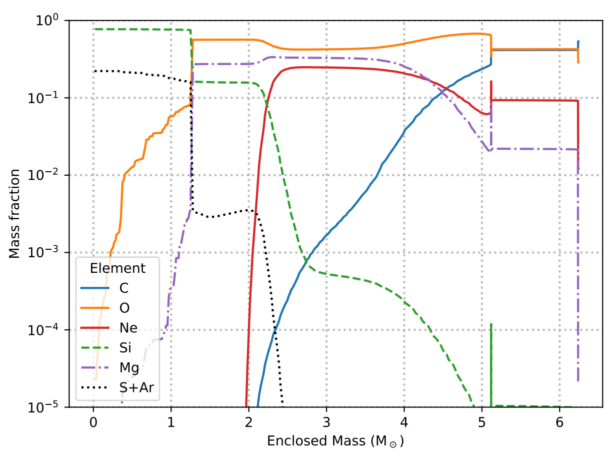

(e) Metamorphic star with $D_{\mathrm{mix,rad}} = 10^5$, pre-collapse chemical radial distribution

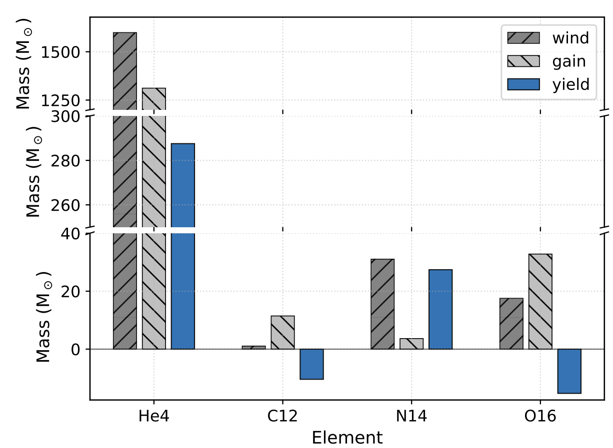

(f) Immortal star, He+CNO yields, peak mass → model end

Figure 5. Metamorphic star's cumulative C, N, and O yields (wind minus gain) with $D_{\mathrm{mix,rad}} = 10^7\,\mathrm{cm^2\,s^{-1}}$ (red) vs $D_{\mathrm{mix,rad}} = 10^5\,\mathrm{cm^2\,s^{-1}}$ (green) during pre and main–sequence phases 1+2 (top left), He-burning phase 3 (top right), and carbon-burning phase 4 (middle left). Pre-collapse mass of various elements and compositional stratification inside a metamorphic star are shown in the middle-right and lower-left panels respectively. Immortal star's steady He and N yield versus C and O drain, accumulated over ≈5 Myrs, are shown in the bottom-right panel. All stellar models use $Y_{\mathrm{d}} = 0.25$, $\lambda_0 = 0.75$, and $\rho_{\mathrm{c}} = 10^{-16}\,\mathrm{g\,cm^{-3}}$.

With the solar values of Y_d and Z_d, we find the N yields to be $\simeq 1.4\,M_\odot$ for $\lambda_0 = 0.50$, $\simeq 3.1\,M_\odot$ for $\lambda_0 = 0.75$, and $\simeq 4.5\,M_\odot$ for $\lambda_0 = 0.90$ during phase 1 and 2 (top panel, Fig. 5). In relative terms this main–sequence period spans 6 Myr, so a single metamorphic star can seed its local zone with more than $0.2 - 0.5\mathrm{M}_\odot$ N on a Myr timescale. Since C+N+O is conserved in the CNO cycle, the positive N yield is accompanied by negative C and O yields during the main sequence evolution, similar to the immortal stars (top panel, Fig. 5).

4.5.3. *Post-main–sequence yields*

However, H–exhaustion in the core leads to the transition to post-main–sequence evolution with He ignition, and the production of C and O in the phase 3 (middle-left panel, Fig. 5). The average mass loss rate $\dot{M} \sim 10^{-5}$–$10^{-4}\,M_\odot\,\mathrm{yr}^{-1}$ (upper panel Fig. 3). Since the stellar envelope is near-Eddington, even increasing nuclear luminosity from the center, the star doesn't impulsively expand into super giants. Instead, it breaks through the outer shells, delivering the bulk of He, H and other elements to the surroundings. The amount of C and O released by the star to the AGN disk depends on the magnitude of $D_\mathrm{mix,rad}$. With a nominal $D_\mathrm{mix,rad} = 10^5\ \mathrm{cm}^2\ \mathrm{s}^{-1}$ (§3.4), elemental diffusion in the outer envelope is limited such that less C and O masses are returned to the disk during the post-main–sequence evolution (phase 3+4, middle-left panel Fig. 5) than they were consumed on the main sequence (phases 1 and 2).

During phase 3, ΔR of the radiative layer is smaller and the triple-α reaction converts He into α-elements on shorter timescale that τ_He. Comparison of yield between models with $D_\mathrm{mix,rad} = 10^5\ \mathrm{cm}^2\ \mathrm{s}^{-1}$ and $10^7\ \mathrm{cm}^2\ \mathrm{s}^{-1}$ indicate that a) the α-element yield increase with $D_\mathrm{mix,rad}$ and b) the latter is adequate for the α-element byproducts in the core to diffuse through the radiative layer, be carried away by the wind and contribute to the stellar yield to the disk. But, in the limit $D_\mathrm{mix,rad} \sim 10^{9-10}\ \mathrm{cm}^2\ \mathrm{s}^{-1}$, there is sufficient mixing for the newly-accreted H–laden disk gas to prolong the shell burning (via CNO-cycle), despite modest $\dot{M}_\mathrm{acc}(\sim 10^{-7} M_\odot\ \mathrm{yr}^{-1})$, to sustain "immortal" post-main–sequence evolution with small residual $M_\star(\lesssim 3M_\odot)$ and thereby prevent the onset of C burning in the core. The enhanced diffusion also enables the replenishment of He and the removal of α-element ashes between the sustained He-burning core and the outer envelope. The C+O byproducts are returned to the disk by the stellar wind. Additional discussion of this outcome will be presented in Xu (2025b, in prep.).

During phase 4, the α-chain reaction converts C and O into Mg and Si byproducts in the core (middle-right panel of Fig 5). For $\lambda_0 = 0.75$ the combined C+O mass fraction drops from 90.78% at He depletion to 55.1% just prior to collapse, while for $\lambda_0 = 0.90$ it falls from 92.9% to 47.5%. The late-stage CO consumption both boosts the eventual yield of intermediate-mass elements (Ne, Mg, and Si) and suppresses the residual C/O ratio.

4.5.4. *Supernova yields.*

With the standard $D_\mathrm{mix,rad}$ prescription, the `MESA` models terminate at the onset of Si burning when central temperature approaches $\simeq 10^{9.5}$K. Substantial masses of Ne, Mg, Si, S remain in the residual core with a surrounding C and O envelope. The core quickly runs out of nuclear fuel and undergoes collapse into either a black hole or a neutron star of a few $M_\odot$. By the pre-collapse stage, Mg and Si together exceed ∼20% of the remaining stellar mass (bottom-left panel (e) Fig.5), S and Ar are poised to rise sharply while Fe-group nuclei, though still $\lesssim 10^{-3}$ by mass before explosive Si burning is ignited.

The stratified composition in the pre-collapse stellar envelope (bottom-left panel Fig.5) determines the relative abundance of the yield (Fryer et al. 2025). With identical D_mix ($= 10^5\ \mathrm{cm}^2\ \mathrm{s}^{-1}$), but different λ_0, the models are similar with each other in the mass-fraction ratios, internal profiles, and overall structure.

MESA's limited nuclear reaction network posts uncertainties on the pre-collapse composition and structure in the core beyond the O/Si-burning phase(Renzo et al. 2024). In a follow-up study, we will use comparison models (Fryer et al. 2025) with more comprehensive treatment of the nuclear reaction network (Woosley et al. 2002; Heger et al. 2005), rotation, magnetic fields, turbulence, and neutrino cooling (Fryer et al. 2018; Andrews et al. 2020) to examine the sensitivity to the choice of reaction networks and diffusion efficiency in MESA.

4.6. *Chemical Yield with Total Retention*

We also consider a set of analogous models under the assumption that, with its yield, the stellar wind contaminates the proximity of the stars which subsequently re-accreted, *in situ*, the polluted gas (§3.3). This effect is particularly important during the prolonged main–sequence evolution (phase 2) when both $\dot{M}_\mathrm{acc}$ and $\dot{M}_\mathrm{wind}$ are higher than $\dot{M}_\mathrm{net}$, i.e. considerable amount of gas is being exchanged with or without net changes in $M_\star$ (Fig. 3).

For stars with "extra mixing", this recycle process is equivalent to chemical insulation which suppress the replenishment of H–rich disk gas. Ali-Dib & Lin (2023) have previously shown and we confirm that nearly total ($\gtrsim 90\%$) retention quenches fresh H supply from the disk to the star (including the nuclear burning core) and leads to transition to metamorphic stars even with extra mixing.

For metamorphic stars (with conventional mixing), $\Delta M_{\rm Z} \sim -M_{\rm max} Z_{\rm d}$ during phase 1 regardless of retention efficiency since the stellar composition has hardly changed. During $\Delta\tau_2$ of main sequence phase 2, total retention is represented by a modified Equation (36) $\Delta M_{\rm Z} = -\int_{\Delta\tau_2} \dot{M}_{\rm net} Z'_\star dt \simeq \tilde{Z}'_\star (M_{\rm max} - M_{\rm collapse})$ where $\tilde{Z}'_\star$ is mass-weighted abundance in the wind-launching outer region of the star. Difference in the nuclear burning rates at each step along the CNO cycle monotonically increases N abundance $Z_{\star,\rm N}$ (and decreases C & O abundance $Z_{\star,\rm C}$ & $Z_{\star,\rm O}$) as $M_\star \to M_{\rm TAMS}$ with $Y_\star \to 1$ (Fig.7 Ali-Dib & Lin, 2023). Consequently,

$$Z'_{\star,\rm N}(M_{\rm max}) \le \tilde{Z}'_\star \le Z'_{\star,\rm N}(M_{\rm TAMS}) \tag{37}$$

and

$$Z'_{\star,\rm C}(M_{\rm max}) \ge \tilde{Z}'_\star \ge Z'_{\star,\rm C}(M_{\rm TAMS}) (\text{also for O}). \tag{38}$$

Since strong stellar wind dominates diminishing accretion during the post main–sequence evolution (phases 3 and 4 in the upper-right and middle-left panels of Fig. 5), such that retention does not significantly contribute to the star's internal composition and $\Delta M_{\rm Z} \simeq \tilde{Z}'_{\star,3+4}(M_{\rm TAMS} - M_{\rm collapse})$ and $\tilde{Z}'_{\star,3+4}$ is mass averaged over phases 3 and 4. Since $M_{\rm max} \gg M_{\rm TAMS}$ and $M_{\rm collapse}$ (Fig 2) $\Delta M_{\rm Z} \simeq (\tilde{Z}'_\star - Z_{\rm d}) M_{\rm max}$.

We adopt $\rho_{\rm c} = 10^{-16}\,{\rm g\,cm^{-3}}$ and $\lambda_0 = 0.75$ which gives $M_{\rm max} = 234 M_\odot$ and $M_{\rm TAMS} = 14.75 M_\odot$. Even if all the C and O mass (based on the disk abundance §3.2) are converted into N during phase 2, the net yield would be $\Delta M_{\rm Z_N} \sim 1.87 M_\odot$ for N, $\Delta M_{\rm Z_C} \sim -0.49 M_\odot$ for C, and $\Delta M_{\rm Z_O} \sim -1.38 M_\odot$. The magnitudes of these quantities are more than half those provided by the zero-retention `MESA` models (lower-right Fig. 5). Since the yield during phases 1, 3, and 4 do not dependent on the retention efficiency, these estimates provide fractionally more positive total C, N, and O yield.

5. SUMMARY AND DISCUSSIONS

Conventional α-model implies AGN disks become gravitationally unstable outside $\sim 10^{2-3} R_\bullet$. Subsequent fragmentation leads to spontaneous *in situ* star formation. Throughout their lifespan, these stars reside in gaseous environment with densities many orders of magnitude greater than that of dense molecular cloud cores. In contrast to the stand-alone massive stars in the field, the embedded stars rapidly gain mass at rates which are self-regulated by the radiative feedback initially from the dissipated accretion energy and subsequently from their intrinsic nucleosynthesis. When they become sufficiently massive, their intrinsic luminosity approaches its Eddington limit, quenches accretion, and drives intense winds to halt further growth.

The limiting stellar mass ($M_{\rm max} \sim$ a few $10^{1-2} M_\odot$) for the onset of this quasi accretion–wind equilibrium increases with the feedback-efficiency factor λ_0 and decreases with helium abundance of the disk gas $Y_{\rm d}$. But it is insensitive to the background density $\rho_{\rm c}$ and sound speed $c_{\rm s}$.

Accretion and wind exchange gas between the disk and stars' surface layer which is separated from their nuclear-burning convective core. While the diffusion coefficient in the convective core has been conventionally estimated using the mixing length model, that of the radiative envelope range from minute molecular values to *ad hoc* prescriptions for "extra mixing" associated with potential rotational circulation or radiative feedback. In view of this uncertain, we presented a series of `MESA` models with a range of mixing efficiency in the radiative envelope.

We show the magnitude of $D_{\rm mix,rad}$ essentially determines the pathways of subsequent evolution (Xu 2025, in press). With an assumed extra mixing for the radiative envelope, the continuous replenishment of H into the core enables immortal stars to produce and release He and N yields with unceasing drainage of C and O from the disk. This expectation is not consistent with the observed super-solar abundance enhancement for all α-element (including C, N, and O), independent of redshift(Huang et al. 2023).

With a conventional diffusivity prescription, the He ashes accumulates in insulated core of main–sequence metamorphic star. These stars shed mass to maintain nearly Eddington limited luminosity and a quasi accretion–wind equilibrium. Concurrent accretion and stellar wind also lead to N yield to and C+O removal from the disk. During the subsequent post-main–sequence evolution, triple-α process leads to the conversion of He into light α elements (mostly C and O) with a positive yields to the disk. In the late stages of stellar evolution, α-chain reaction converts the light into heavy α elements with chemically stratified stellar structure. The metamorphic stars undergo supernova and return most of the residual C and O in the envelope as well as some Mg and Si in the core and Fe produced in circumstellar disks around their compact remnants. Metamorphic stars' prolific and robust produce of heavy elements are in general agreement with the observed super-solar α-elements and sub-solar Fe abundances of AGN BLRs (Huang et al. 2023). The differential magnitude of individual elements' yield depends primarily the diffusivity during the post main–sequence evolution and star's pre-collapse angular momentum distribution.

Based on their evolution track, we extrapolate the metamorphic stars' mass function and surface density $s_\star$ required to maintain a state of marginal gravitational (in)stability for the AGN disk. Metamorphic stars continually form at a self-regulated rate as their evolve (on a few Myr timescale) into stellar mass (a few $M_\odot$) compact remnants. In a follow-up paper, we will infer, from AGN's observed slightly subsolar Fe abundance, the production rate and evolution of stellar-mass black-hole population.

This unceasing self-regulated star formation efficiency fundamentally differs from that of stand-along star forming regions in the Galaxy. Moreover, the heavy-element yields are deposited into the AGN disks and join the accretion flow toward the central supermassive black holes. Since these pollutants do not accumulate over time, the metallicity of the BLRs reach a saturation level which is independent of the cosmic redshift (Huang et al. 2023). This mechanism differs from the traditional explanation of high quasar metallicities (which often invokes an earlier phase of starburst and enrichment in the host galaxy) by placing the enrichment process *in situ* within the AGN–disk. Detailed analysis on the chemical evolution of AGN disks will be presented in subsequent works.

Finally, the high $s_\star$ of coexisting metamorphic stars also implies frequent merger events between them, especially in the inner regions of the disk. The coalescence of main–sequence metamorphic stars modifies their $Y_\star$ and reset their evolutionary course. If the merger timescale $\tau_{\rm merger} \lesssim \tau_\star$, these stars would be continually rejuvenated and preserved as "immortal" stars despite the $Y_\star$ enrichment and mass shading between merger episodes. These processes will also be analyzed in subsequent investigations along with the possibility of the capture of black holes by metamorphic stars. The possibility of co-existing "immortal" stars at small disk radii and metamorphic stars further out may be potentially observable by measuring the abundance gradient of α-elements in the BLRs of violent variable and changing-look AGNs. This attempt is ongoing (Huang et al, in preparation) and its finding will be presented elsewhere.

It is worth noting that in the very dense inner regions of the disk where $\tau_{\rm merge} \lesssim \tau_{\rm wind}$ (Eq. 23), stars coalesce before they can re-establish a quasi hydrostatic equilibrium, undergo runaway growth beyond $10^3 M_\odot$. The embedded very-massive stars(VMS) scenario also has implication for transient phenomena in AGNs. For instance, if one of these massive stars undergoes a supernova, it would occur deeply embedded in the AGN–disk. The interaction of supernova ejecta with the dense disk gas could lead to a shock breakout signature or a luminous radio afterglow observable in conjunction with an AGN. There has been speculation that some unusual transient events in galactic nuclei (sometimes labeled as "changing-look AGN" or peculiar nuclear flares) might be attributed to stellar transients within disks. Our study provides a concrete model for one class of such events.

Software: MESA (Paxton et al. 2011, 2013, 2015, 2019, 2018; Jermyn et al. 2023), NumPy (Harris et al. 2020), matplotlib (Hunter 2007)

DATA AVAILABILITY

All simulation data, inlists, custom routines, and output used in this work are available at https://github.com/zhxu-astro/AGNstarRadFB.

ACKNOWLEDGMENTS

The authors thank Mohamad Ali-Dib, Chris Fryer, Stan Woosley, Long Wang, Jiamu Huang, Sunny Wong, Keith Horne, Jeremy Goodman, and Yan-Fei Jiang for useful conversations. This research received no external funding.

REFERENCES

Ali-Dib, M., & Lin, D. N. C. 2023, MNRAS, 526, 5824, doi: 10.1093/mnras/stad2774

Andrews, S., Fryer, C., Even, W., Jones, S., & Pignatari, M. 2020, ApJ, 890, 35, doi: 10.3847/1538-4357/ab64f8

Angulo, C., Arnould, M., Rayet, M., et al. 1999, NuPhA, 656, 3, doi: 10.1016/S0375-9474(99)00030-5

Artymowicz, P., Lin, D. N. C., & Wampler, E. J. 1993, ApJ, 409, 592, doi: 10.1086/172690

Blouin, S., Shaffer, N. R., Saumon, D., & Starrett, C. E. 2020, ApJ, 899, 46, doi: 10.3847/1538-4357/ab9e75

Cantiello, M., Jermyn, A. S., & Lin, D. N. C. 2021, ApJ, 910, 94, doi: 10.3847/1538-4357/abdf4f

Cassisi, S., Potekhin, A. Y., Pietrinferni, A., Catelan, M., & Salaris, M. 2007, ApJ, 661, 1094, doi: 10.1086/516819

Chen, Y.-X., Jiang, Y.-F., & Goodman, J. 2025, arXiv e-prints, arXiv:2505.13951, doi: 10.48550/arXiv.2505.13951

Chen, Y.-X., Jiang, Y.-F., Goodman, J., & Lin, D. N. C. 2024, ApJ, 974, 106, doi: 10.3847/1538-4357/ad6dd4

Chen, Y.-X., Jiang, Y.-F., Goodman, J., & Ostriker, E. C. 2023, ApJ, 948, 120, doi: 10.3847/1538-4357/acc023

Chen, Y.-X., & Lin, D. N. C. 2024, ApJ, 967, 88, doi: 10.3847/1538-4357/ad3c3a

Chugunov, A. I., Dewitt, H. E., & Yakovlev, D. G. 2007, PhRvD, 76, 025028, doi: 10.1103/PhysRevD.76.025028

Cyburt, R. H., Amthor, A. M., Ferguson, R., et al. 2010, ApJS, 189, 240, doi: 10.1088/0067-0049/189/1/240

Dittmann, A. J., Cantiello, M., & Jermyn, A. S. 2021, ApJ, 916, 48, doi: 10.3847/1538-4357/ac042c

Fabj, G., Dittmann, A. J., Cantiello, M., Perna, R., & Samsing, J. 2025, ApJ, 981, 16, doi: 10.3847/1538-4357/ada896

Ferguson, J. W., Alexander, D. R., Allard, F., et al. 2005, ApJ, 623, 585, doi: 10.1086/428642

Fryer, C. L., Andrews, S., Even, W., Heger, A., & Safi-Harb, S. 2018, ApJ, 856, 63, doi: 10.3847/1538-4357/aaaf6f

Fryer, C. L., Huang, J., Ali-Dib, M., et al. 2025, MNRAS, 537, 1556, doi: 10.1093/mnras/staf130

Fuller, G. M., Fowler, W. A., & Newman, M. J. 1985, ApJ, 293, 1, doi: 10.1086/163208

Goodman, J., & Tan, J. C. 2004, ApJ, 608, 108, doi: 10.1086/386360

Graham, M. J., Ford, K. E. S., McKernan, B., et al. 2020, PhRvL, 124, 251102, doi: 10.1103/PhysRevLett.124.251102

Hamann, F., & Ferland, G. 1999, ARA&A, 37, 487, doi: 10.1146/annurev.astro.37.1.487

Hamann, F., Korista, K. T., Ferland, G. J., Warner, C., & Baldwin, J. 2002, ApJ, 564, 592, doi: 10.1086/324289

Harris, C. R., Millman, K. J., van der Walt, S. J., et al. 2020, Nature, 585, 357, doi: 10.1038/s41586-020-2649-2

Heger, A., Woosley, S. E., & Spruit, H. C. 2005, ApJ, 626, 350, doi: 10.1086/429868

Huang, J., Lin, D. N. C., & Shields, G. 2023, MNRAS, 525, 5702, doi: 10.1093/mnras/stad2642

Hunter, J. D. 2007, Computing in Science and Engineering, 9, 90, doi: 10.1109/MCSE.2007.55

Iglesias, C. A., & Rogers, F. J. 1996, ApJ, 464, 943, doi: 10.1086/177381

Itoh, N., Hayashi, H., Nishikawa, A., & Kohyama, Y. 1996, ApJS, 102, 411, doi: 10.1086/192264

Jermyn, A. S., Dittmann, A. J., McKernan, B., Ford, K. E. S., & Cantiello, M. 2022, ApJ, 929, 133, doi: 10.3847/1538-4357/ac5d40

Jermyn, A. S., Schwab, J., Bauer, E., Timmes, F. X., & Potekhin, A. Y. 2021, ApJ, 913, 72, doi: 10.3847/1538-4357/abf48e

Jermyn, A. S., Bauer, E. B., Schwab, J., et al. 2023, ApJS, 265, 15, doi: 10.3847/1538-4365/acae8d

Jiang, Y.-F., & Goodman, J. 2011, ApJ, 730, 45, doi: 10.1088/0004-637X/730/1/45

Lamers, H. J. G. L. M., & Cassinelli, J. P. 1999, Introduction to Stellar Winds

MacLeod, M., & Lin, D. N. C. 2020, ApJ, 889, 94, doi: 10.3847/1538-4357/ab64db

Maeder, A., & Meynet, G. 2010, NewAR, 54, 32, doi: 10.1016/j.newar.2010.09.017

McKernan, B., Ford, K. E. S., Lyra, W., & Perets, H. B. 2012, MNRAS, 425, 460, doi: 10.1111/j.1365-2966.2012.21486.x

Nagao, T., Maiolino, R., & Marconi, A. 2006, A&A, 459, 85, doi: 10.1051/0004-6361:20065216

Oda, T., Hino, M., Muto, K., Takahara, M., & Sato, K. 1994, Atomic Data and Nuclear Data Tables, 56, 231, doi: 10.1006/adnd.1994.1007

Owocki, S. P., & Shaviv, N. J. 2012, in Astrophysics and Space Science Library, Vol. 384, Eta Carinae and the Supernova Impostors, ed. K. Davidson & R. M. Humphreys, 275, doi: 10.1007/978-1-4614-2275-4_12

Paxton, B., Bildsten, L., Dotter, A., et al. 2011, ApJS, 192, 3, doi: 10.1088/0067-0049/192/1/3

Paxton, B., Cantiello, M., Arras, P., et al. 2013, ApJS, 208, 4, doi: 10.1088/0067-0049/208/1/4

Paxton, B., Marchant, P., Schwab, J., et al. 2015, ApJS, 220, 15, doi: 10.1088/0067-0049/220/1/15

Paxton, B., Schwab, J., Bauer, E. B., et al. 2018, ApJS, 234, 34, doi: 10.3847/1538-4365/aaa5a8

Paxton, B., Smolec, R., Schwab, J., et al. 2019, ApJS, 243, 10, doi: 10.3847/1538-4365/ab2241

Poutanen, J. 2017, ApJ, 835, 119, doi: 10.3847/1538-4357/835/2/119

Prat, V., & Lignières, F. 2014, Astronomy & Astrophysics, 566, A110, doi: 10.1051/0004-6361/201423655

Renzo, M., Goldberg, J. A., Grichener, A., Gottlieb, O., & Cantiello, M. 2024, Research Notes of the American Astronomical Society, 8, 152, doi: 10.3847/2515-5172/ad530e

Samsing, J., Bartos, I., D'Orazio, D. J., et al. 2022, Nature, 603, 237, doi: 10.1038/s41586-021-04333-1

Shankar, F., Weinberg, D. H., & Miralda-Escudé, J. 2009, ApJ, 690, 20, doi: 10.1088/0004-637X/690/1/20

Sirko, E., & Goodman, J. 2003, MNRAS, 341, 501, doi: 10.1046/j.1365-8711.2003.06431.x

Spruit, H. C. 2002, A&A, 381, 923, doi: 10.1051/0004-6361:20011465

Tagawa, H., Haiman, Z., & Kocsis, B. 2020, ApJ, 898, 25, doi: 10.3847/1538-4357/ab9b8c

Thompson, T. A., Quataert, E., & Murray, N. 2005, ApJ, 630, 167, doi: 10.1086/431923

Wang, S., Jiang, L., Shen, Y., et al. 2022, ApJ, 925, 121, doi: 10.3847/1538-4357/ac3a69

Wang, Y., Zhu, Z., & Lin, D. N. C. 2024, MNRAS, 528, 4958, doi: 10.1093/mnras/stae321

Woosley, S. E., Heger, A., & Weaver, T. A. 2002, Reviews of Modern Physics, 74, 1015, doi: 10.1103/RevModPhys.74.1015

Xu, F., Bian, F., Shen, Y., et al. 2018, MNRAS, 480, 345, doi: 10.1093/mnras/sty1763

Yu, Q., & Tremaine, S. 2002, MNRAS, 335, 965, doi: 10.1046/j.1365-8711.2002.05532.x

Zhang, C., Wu, Q., Fan, X., et al. 2025, arXiv e-prints, arXiv:2505.12719, doi: 10.48550/arXiv.2505.12719